Advances in Science and Technology Research Journal

Advances in Science and Technology Research Journal, 2025, 19(9), 237–253
https://doi.org/10.12913/22998624/207297
ISSN 2299-8624, License CC-BY 4.0

Received: 2025.06.12
Accepted: 2025.07.15
Published: 2025.08.01

The studies of low-cycle fatigue behavior of high manganese TWIP steel

Grzegorz Junak[1], Magdalena Barbara Jabłońska[2]*

[1] Silesian University of Technology, ul. Akademicka 2A, 44-100 Gliwice, Poland
[2] Łukasiewicz Research Network, Institute of Non Ferrous Metals, ul. Sowińskiego 5, 44-100 Gliwice, Poland
* Corresponding author's e-mail: magdalena.jablonska@icloud.com

ABSTRACT

The article, explores the fatigue performance of a high-manganese TWIP steel under low-cycle fatigue conditions. The researchers aimed to address a gap in the existing literature by systematically analysing the role of mechanical twinning in the fatigue resistance of TWIP steel under different strain regimes. Fatigue tests were conducted in three modes: oscillating strain (tension-compression), positive-only strain and negative-only strain. These tests were performed at various strain amplitudes ranging from 0.6% to 1.2%. Their results revealed pronounced asymmetry in fatigue behavior. The steel exhibited optimal performance under compressive (negative) strain and suboptimal performance under tensile (positive) strain, indicating greater sensitivity to tension during cyclic loading. At lower strain amplitudes, the material exhibited extended stabilisation with minimal damage accumulation. At higher strain levels, cyclic hardening was observed, particularly under oscillating and positive strain conditions. Manson–Coffin analysis showed that strength properties dominated fatigue life under oscillating loading, whereas plastic deformation played a more significant role under unidirectional strain modes. Fractographic analysis confirmed the material's high ductility, revealing classic ductile failure features such as dimples and striations across all test conditions. Microstructural observations revealed that twinning occurred uniformly at lower strains but became more localised and intense near fracture zones at higher strains. These areas also exhibited increased hardness, linking localised twinning activity to material strengthening during cyclic deformation.

Keywords: TWIP steels, fatigue behaviour, mechanical twinning, ductility.

INTRODUCTION

Fe-Mn-Al-C steels, a subclass of Advanced High-Strength Steels (AHSS), are renowned for their exceptional combination of mechanical properties, such as high specific strength, ductility, and reduced density [1]. These attributes, along with high strain hardening capacity, corrosion resistance, and energy absorption, make them highly suitable for applications in the automotive, aerospace, mining, and chemical industries [2, 3, 4]. Their outstanding plastic behavior is largely governed by deformation mechanisms like twinning-induced plasticity (TWIP), activated within a specific stacking fault energy (SFE) range-typically between 20 and 40 mJ/m² [5]. By the presence of lightweight elements such as Al and C, which not only decrease the average atomic mass but also expand the lattice parameter, the reduction in density achieved in specific grades of TWIP steels improves energy efficiency through vehicle weight reduction, which is a key objective [6, 7, 8, 9]. Aluminum, a key alloying element in Fe-Mn-Al-C steels, reduces density while increasing the SFE, potentially suppressing deformation twinning and altering the dominant plasticity mechanism toward planar slip [10]. Despite these alloys' high potential for dynamic loading conditions, particularly in weight-sensitive automotive structures, a noticeable gap remains in the literature regarding their full fatigue performance, especially in low-cycle fatigue (LCF) regimes where high plastic strain amplitudes are present [11]. While

numerous studies have explored the generally fatigue behavior, mechanical behavior of TWIP steels and their deformation mechanisms, LCF investigations remain fragmented and often inconclusive [12, 13]. Some studies such report inconsistent findings: some observe a lack of deformation twinning under cyclic loading, while others identify its presence, indicating that the role of TWIP in fatigue resistance is still not well understood [18, 14, 15]. Moreover, the absence of twins during cyclic loading has also been reported by other researchers, although some have identified them, revealing that the fatigue behavior of these steels is not yet well understood. Additionally, since in the literature the first news report evaluated the fatigue performance of TWIP steels by Cornette et al. [16], other researchers have reported varying fatigue limit values depending on the applied stress ratio R (YS) [17]. Fatigue limits of about 400 MPa were measured for R = -1 [16] and 260 MPa for R = 0.1 [18], both expressed in terms of stress amplitude. The fatigue limit for R = 0.1 to ultimate tensile strength (YS/UTS) ratio is around 0.2 [20]. This ratio is lower for TWIP steels than the ones obtained for other AHSS of similar strength, such as values larger than 0.25 [19, 20]. Such a ratio for TWIP steels is similar to the one found for austenitic stainless steels or press-hardening steels (PHS) [21]. Such a low YS/UTS ratio for TWIP steels has stimulated the research to improve their high cycle fatigue (HCF) resistance. It is accepted that the general enhancement of the HCF resistance comes from the presence of twins induced by pre-straining the material. However, the ultimate tensile strength (YS/UTS) ratio analyzed by authors has a much higher value. Such values indicate a very high yield strength of TWIP steels and give promising results for indicating these steels as one of the more stable during cyclic fatigue. In this context, however, some research give informations about the fatigue behaviour of TWIP steels even in those research, there remains a lack of extensive, systematic LCF testing across a broad range of strain amplitudes and stress ratios, which is essential for accurately characterizing the cyclic response and life prediction of these materials under realistic service conditions, what kind of research has been conducted multiple times across a broad spectrum of structural steel [22, 23]. This study aims to address this knowledge gap by examining the cyclic behavior of Fe-Mn-Al-C steels, with particular attention to the fatigue ratio analysis in the context of activation or suppression of TWIP mechanisms under cyclic loading. The objective is to determine how twinning contributes (or fails to contribute) to fatigue resistance in the LCF regime, thereby informing design decisions for components subjected to dynamic loads. Moreover, the microstructures and fractographic analysis were performed to find some phenomena regarding the development of the share of twinning during the cyclic load.

MATERIAL AND METHODOLOGY

Material

The material for testing was high-manganese steel with the chemical composition shown in Tab.1. The content of individual chemical elements was designed to obtain the assumed value of SFE between 20 and 40 mJ/m². The steel was produced by the hot rolling process and subjected to solution heat treatment from a temperature of 1100 °C/2h and water cooling. The assumed chemical composition of the steel provided a single-phase austenitic structure, which was consistent with the adopted assumptions. In addition to typical TWIP steel additives such as C, Mn, and Al, the Ce additive for strengthening the grain boundary, absorbing impurities such as Ca and S and reduces the interface energy for driving grain growth and increasing the density of geometrically necessary dislocations has been implemented [24]. The average hardness of the undeformed material was 160.5 HV1.

Static tensile tests

To determine the basic mechanical properties of X60MnAl20-3 steel, static tensile tests were carried out at room temperature. The tests were carried out on a servohydraulic MTS-810 machine equipped with a digital control system TestSTAR II and TestWARE SX, giving the possibility of recording data from individual control channels. The tests were carried out following PN-EN ISO 6892-1. The static characteristics are shown in Figures 1–3. Figure 4 shows the microstructure of the tested steel in initial state (after solutioning).

It was observed that the steel has a high level of plastic properties: elongation at 65% and constriction at 68%. At the same time, the steel

Table 1. Chemical composition of X60MnAl20-3 [% mas.]

Grade X60MnAl20-3	Chemical composition, % wt.									
	C	Mn	Al	P	S	Mo	B	Ce La Nd	N ppm	Fe
Smelting analysis	0.590	20.08	5.30	<0.005	<0.006	0.16	0.002	0.03 0.016 0.014	24	Balance

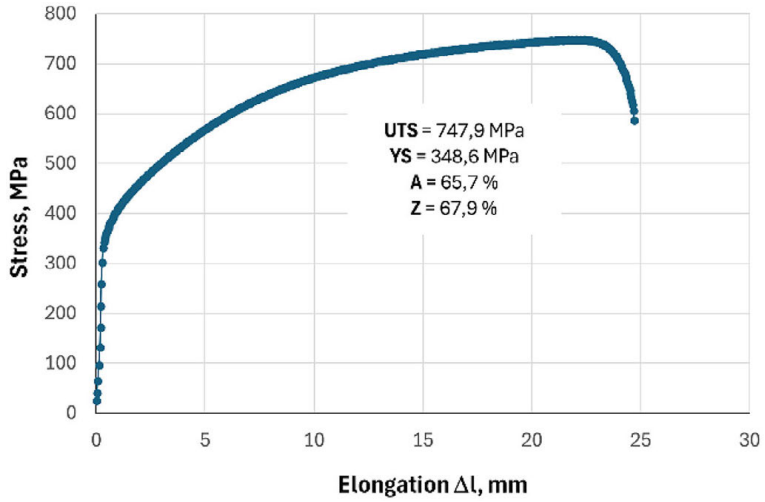

Figure 1. Static tensile characteristics of X60MnAl20-3 steel

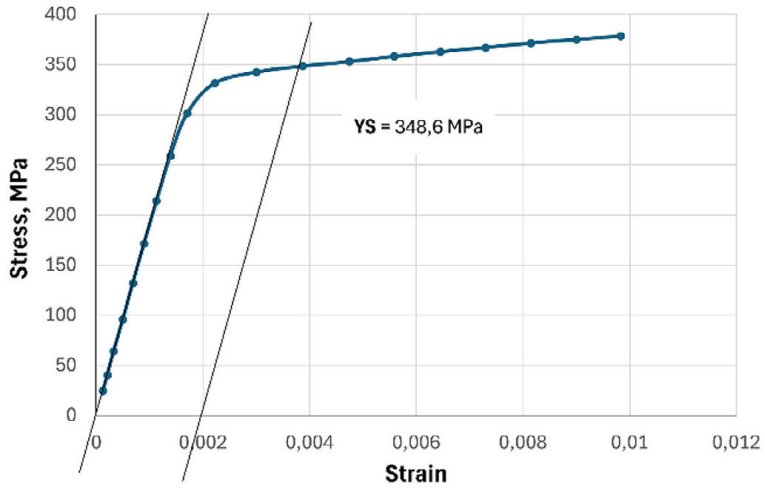

Figure 2. Static tensile characteristics with accurate elongation measurement of X60MnAl20-3 steel

has high strength properties with a high yield strength: UTS = 748 MPa, YS/UTS = 0.47. This guarantees stable operation even when the yield strength is significantly exceeded.

Fatigue low cycles tests (LCF)

Fatigue tests were carried out over a range of a small number of cycles. They were also conducted on an MTS-810 machine at room temperature. The testing program was divided into three main stages as shown in Figure 5.

1. Fatigue tests for oscillating cycles – STAGE I (Specimen A),
2. Fatigue tests for cycles implemented only in the range of positive deformation – STAGE II (Specimen B),
3. Fatigue tests for cycles implemented

exclusively in the range of negative deformation – STAGE III (Specimen C).

Strain control was applied using an MTS-653-11c-20 extensometer with a measuring base of 25mm. For each stage, tests were implemented at a constant level of the total strain range: 0.6%, 0.7%, 0.8%, 1.0%, 1.2%. The frequency of change of loading cycles was in the range of 0.05÷0.2 Hz. During the tests, data were recorded from individual control channels: displacement, force, strain. Data recording occurred every 0.5s. The recorded data allowed the preparation of fatigue characteristics depicting the behavior of X60MnAl20-3 steel at each test stage. Fatigue life characteristics, cyclic deformation plots, cyclic strengthening plots and Manson-Coffin life plots were determined for each of the stages carried out.

This work used pendulum and other cycles (positive and negative). An innovative approach to the destruction process was strain control. The goal of the research was to accurately reflect the behavior of the steel under study in real conditions. The idea was to study how the steel behaves under deformation (positive and negative), which does not necessarily translate into the resulting stresses. From the point of view of applying the steel under study, this approach may better reflect real conditions.

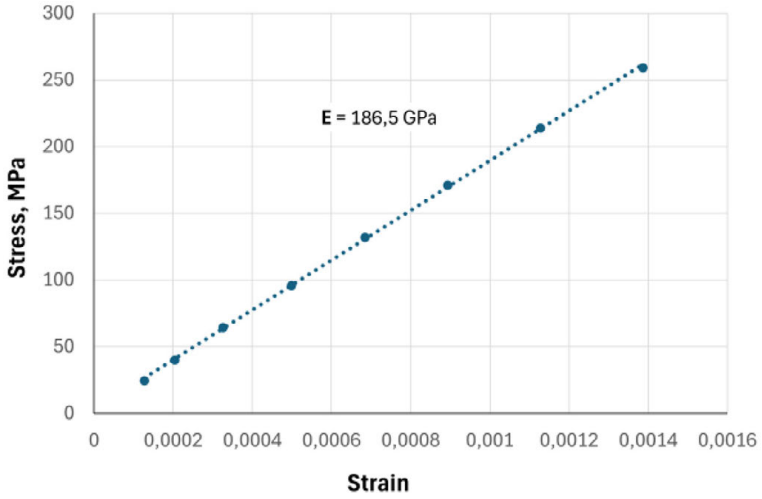

Figure 3. Characteristics showing the longitudinal modulus of elasticity of X60MnAl20-3 steel (Young's modulus)

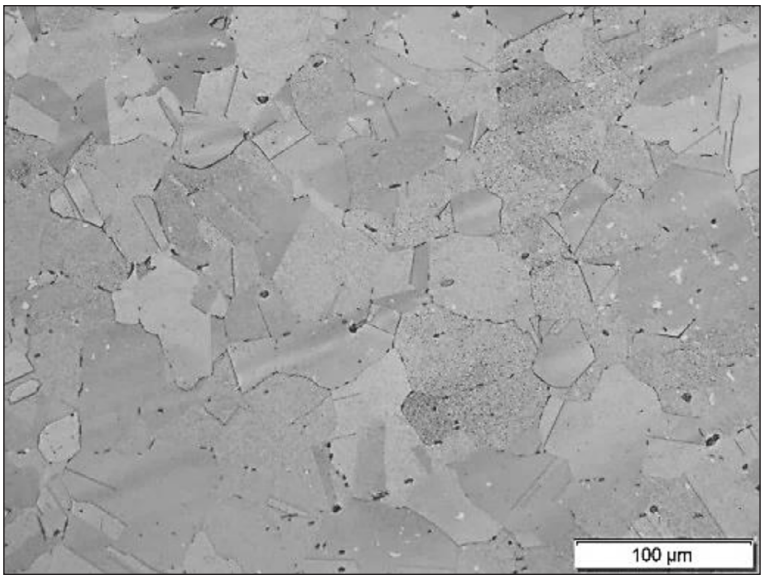

Figure 4. Microstructure of X60MnAl20-3 steel – initial state

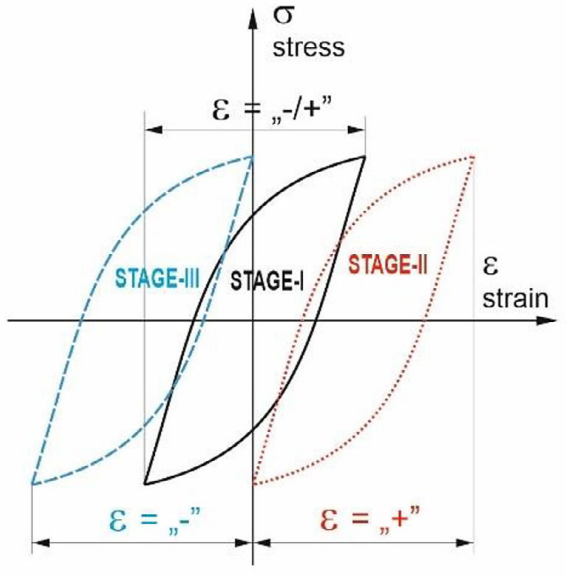

Figure 5. Schematic representation of the division of implemented fatigue tests due to the course of deformation (own studies)

The hardness of the tested steel was measured on the samples in the initial state, after static tensile tests, and after fatigue tests by the Vickers method using a ZWICK Roel ZHU hardness tester. Hardness was measured on the longitudinal fillet at a distance of about 0.5 mm from the breakthrough (Fig. 6).

The microstructure was investigated using a Keyence VHX-7000 digital microscope. The samples were prepared by grinding with SiC water paper with gradations ranging from 800 to 4,000, and then polishing with Struers polishing cloths and diamond suspensions with gradations ranging from 9 to 1 micrometre. Scanning transmission electron microscopy (Zeiss Gemini Leo 1525) was used for fractographic observations.

RESULTS AND DISCUSSION

Fatigue test results

For each of the test stages carried out, characteristics were prepared showing the behavior of the material during testing at the corresponding range of $\Delta\varepsilon_t$ total strain (hysteresis loops), as well as summary characteristics showing the behavior of the material subjected to testing corresponding to a particular stage. Selected characteristics developed for a particular test stage are presented at Figures 7÷21. Tables 2÷4 show the parameters recorded for each range of total strain $\Delta\varepsilon_t$.

After analyzing the results of the low-cycle fatigue tests conducted during all three stages of testing, it was concluded that X60MnAl20-3 steel, when subjected to fatigue tests at negative values of total strain, exhibited the highest fatigue life, or the number of cycles to failure. In contrast, steel subjected to fatigue tests at positive total strain values had the highest durability (Figure 22). These results suggest that the analyzed type is much more sensitive to positive strain than negative strain in terms of failure. This is particularly noticeable at low levels of total strain 0.6–0.7% (Fig. 22).

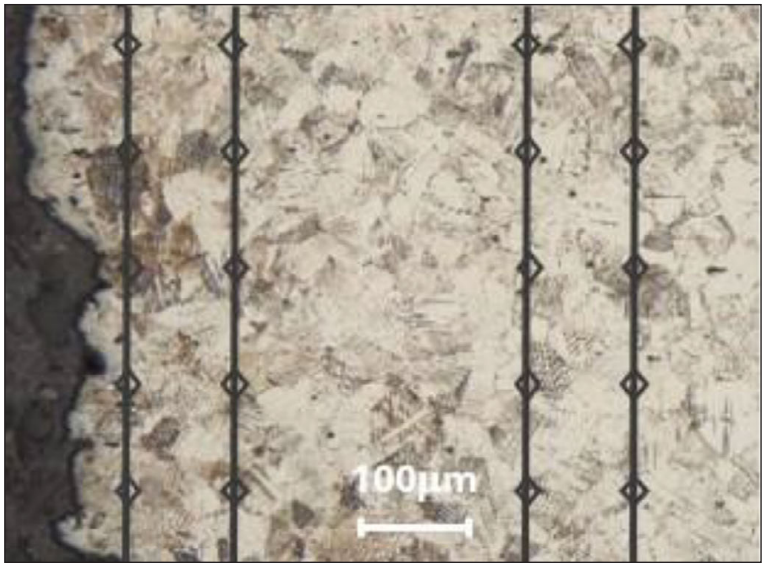

Figure 6. Schematic showing hardness measurement locations on the deposit after fatigue testing

Table 2. Characteristic parameters recorded and determined during tests for oscilating cycles

Specimen idnetification	Total strain range $\Delta\varepsilon_t$	Elastic strain range $\Delta\varepsilon_e$	Plastic strain range $\Delta\varepsilon_p$	Saturation stress σ_n	Number of cycle to failure N_f
Pr-1A	0.0060	0.003537	0.002463	301.6	22400
Pr-2A	0.0070	0.003395	0.003605	313.6	18600
Pr-3A	0.0080	0.003739	0.004261	322.5	8420
Pr-4A	0.0100	0.003957	0.006043	366.8	3100
Pr-5A	0.0120	0.004402	0.007598	416.7	1660

Characteristics determined for fatigue tests performed with oscillating cycles - STAGE I.

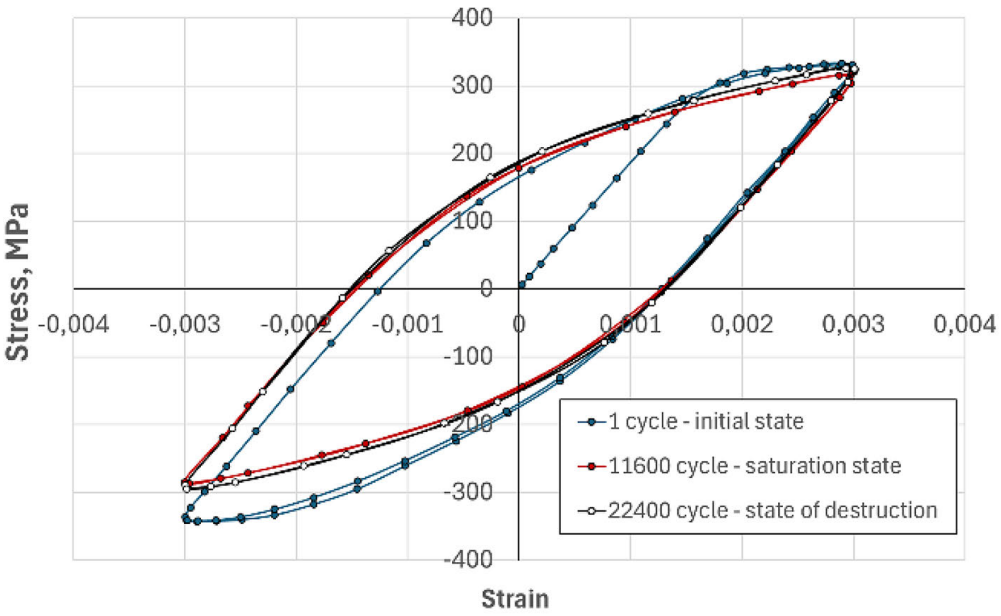

Figure 7. Characteristic hysteresis loops recorded at room temperature for a strain range of 0.6% – oscilating cycles

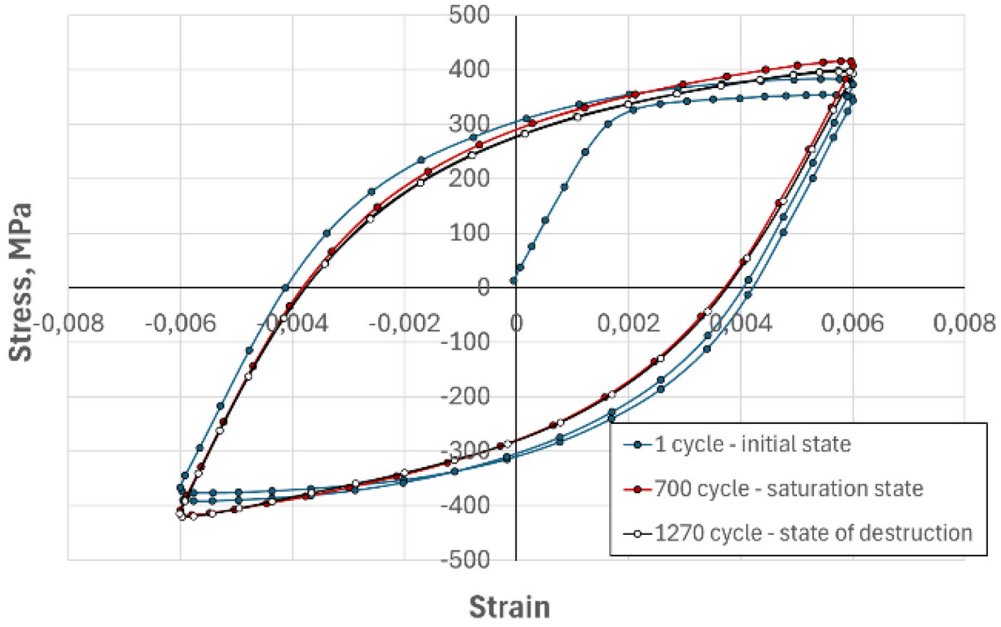

Figure 8. Characteristic hysteresis loops recorded at room temperature for a strain range of 1.2% – oscilating cycles

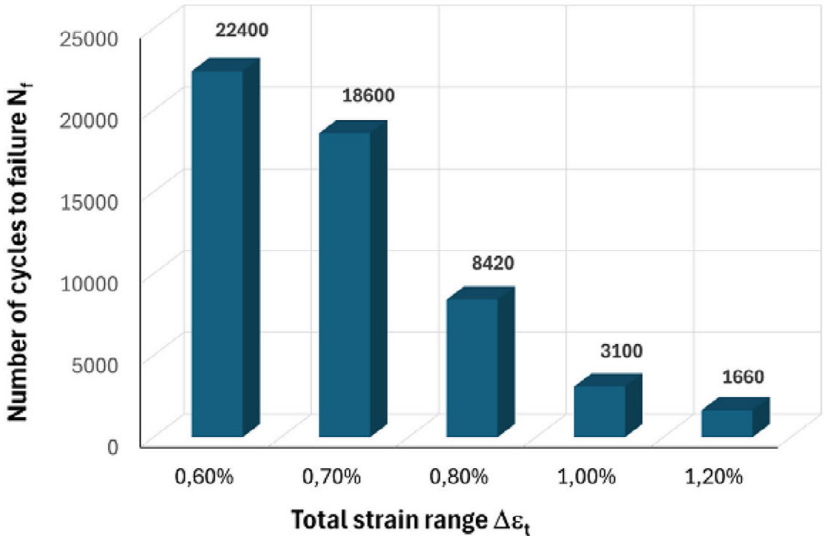

Figure 9. Fatigue life graph as number of cycles to failure – oscilating cycles

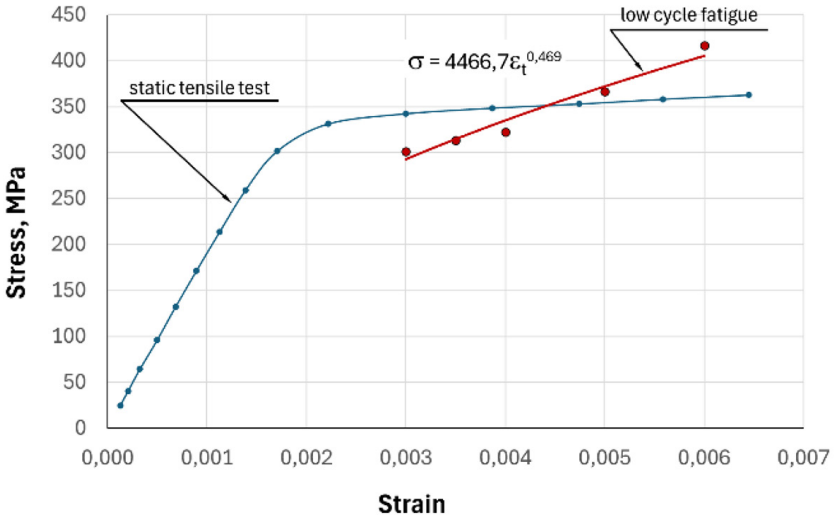

Figure 10. Cyclical strengthening chart – oscilating cycles

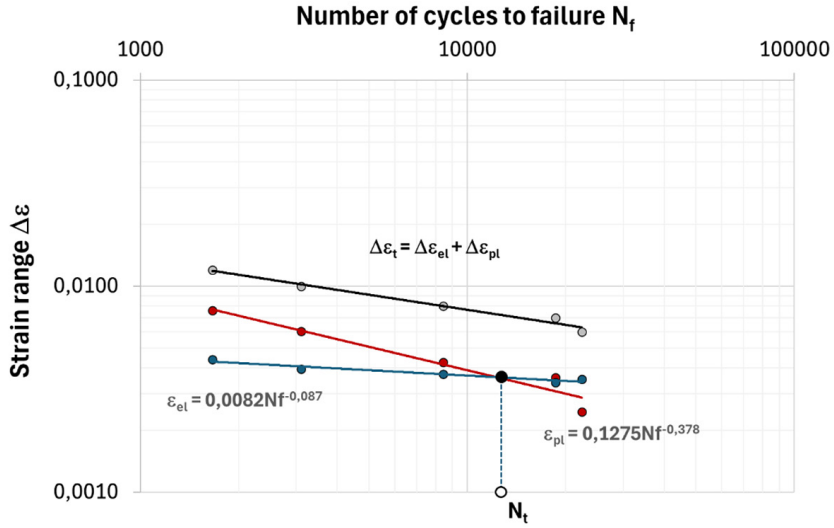

Figure 11. Fatigue life graph in the Manson-Coffin system – oscilating cycles

Table 3. Characteristic parameters recorded and determined during tests performed at a positive level of total strain

Specimen idnetification	Total strain range $\Delta\varepsilon_t$	Elastic strain range $\Delta\varepsilon_e$	Plastic strain range $\Delta\varepsilon_\pi$	Saturation stress σ_v	Number of cycle to failure N_f
Pr-1B	0.0060	0.002617	0.003383	297.7	14750
Pr-2B	0.0070	0.003623	0.003377	313.9	11350
Pr-3B	0.0080	0.004388	0.003612	327.8	6060
Pr-4B	0.0100	0.005949	0.004051	364.9	2450
Pr-5B	0.0120	0.007276	0.004724	413.1	990

Characteristics determined for fatigue tests performed with positive total strain - STAGE II.

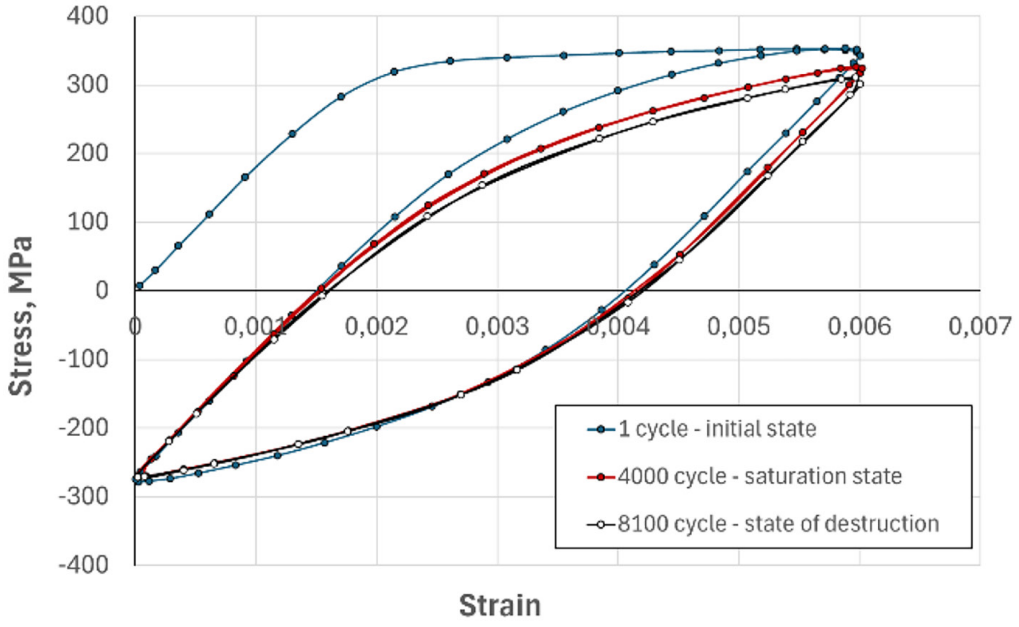

Figure 12. Characteristic hysteresis loops recorded at room temperature for a strain range of 0.6% – positive cycles

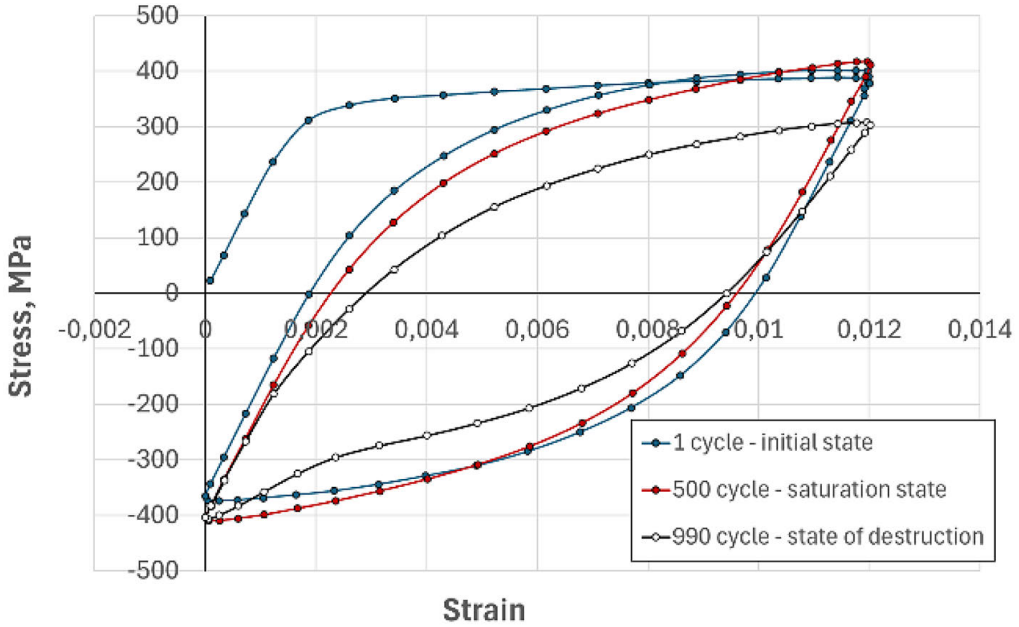

Figure 13. Characteristic hysteresis loops recorded at room temperature for a strain range of 0.6% – positive cycles

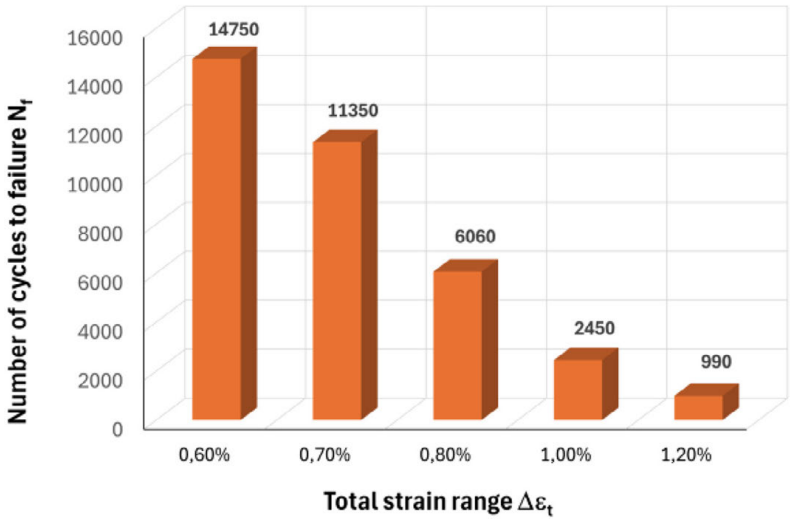

Figure 14. Fatigue life graph as a number of cycles to failure – positive values of total strain

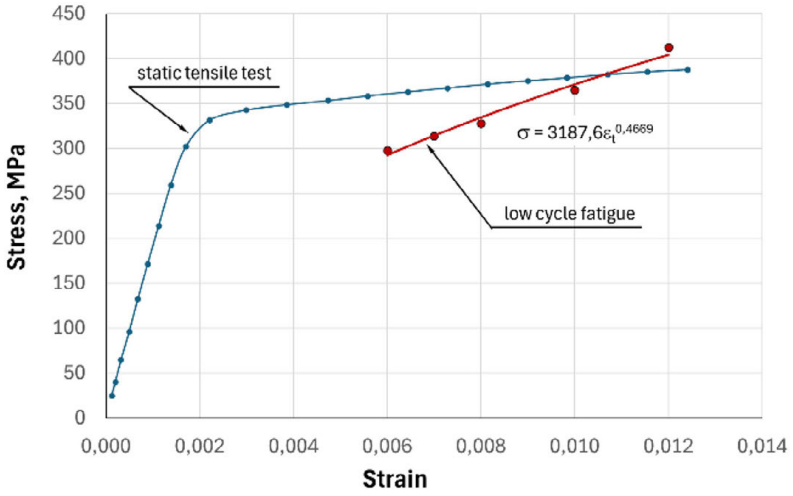

Figure 15. Cyclical strengthening chart – positive values of total strain

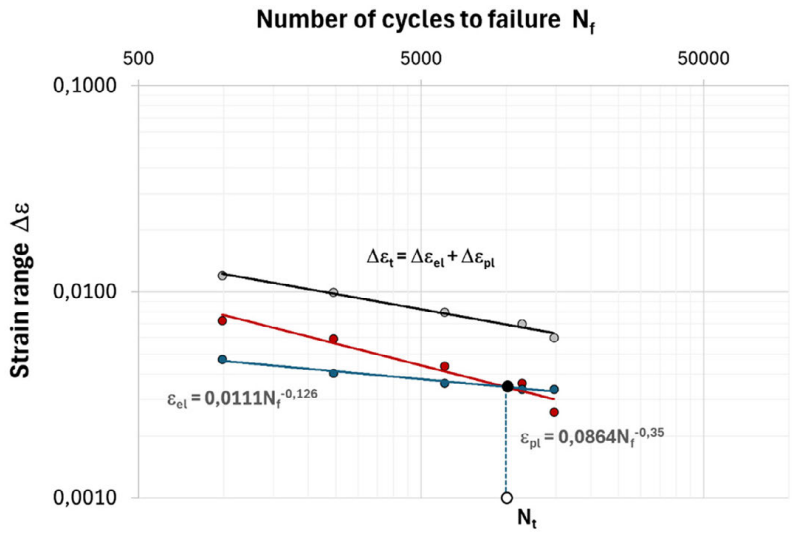

Figure 16. Fatigue life graph in the Manson-Coffin system – positive values of total strain
Characteristics determined for fatigue tests performed with negative total strain – STAGE III.

Table 4. Characteristic parameters recorded and determined during tests carried out at a negative level of total strain

Sample indentification	Total strain range $\Delta\varepsilon_X$	Elastic strain range $\Delta\varepsilon_\varepsilon$	Plastic strain range $\Delta\varepsilon_\pi$	Saturation stress σ_v	Number of cycle to failure N_f
Pr-1C	0.0060	0.003176	0.002824	308.9	32280
Pr-2C	0.0070	0.003520	0.003480	313.0	29200
Pr-3C	0.0080	0.003644	0.004356	332.3	8750
Pr-4C	0,0100	0.004053	0.005947	363.7	2850
Pr-5C	0.0120	0.004492	0.007508	380.1	1740

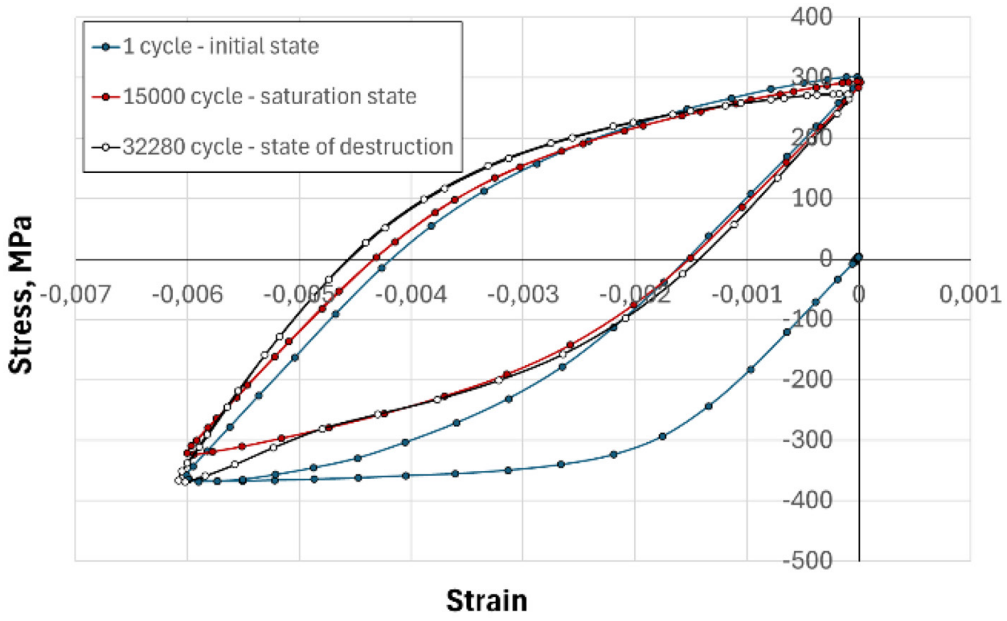

Figure 17. Characteristic hysteresis loops recorded at room temperature for the strain range of 0.6% – negative strain

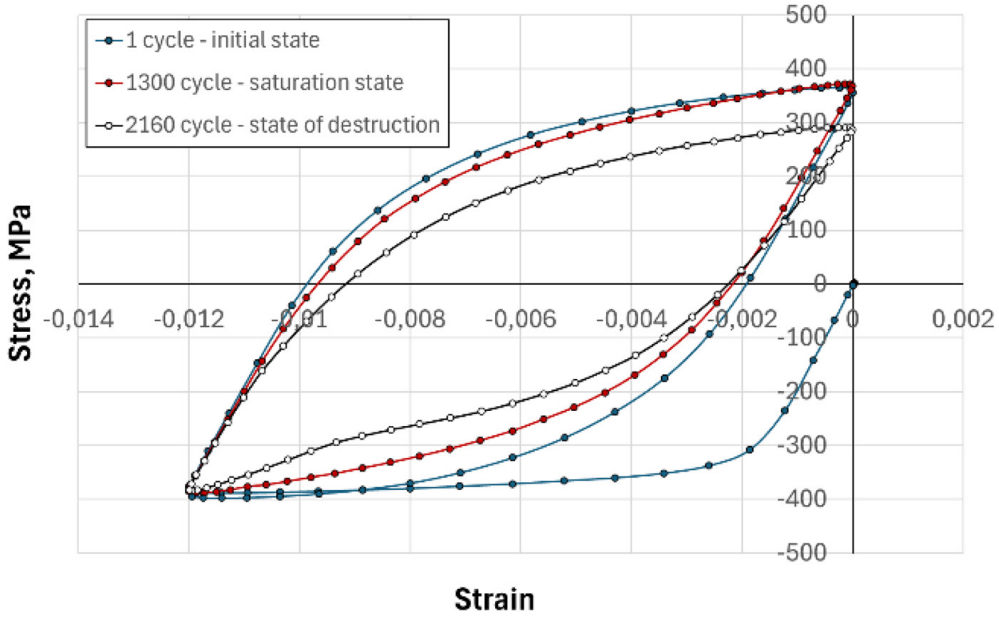

Figure 18. Characteristic hysteresis loops recorded at room temperature for the strain range of 1.2%. – negative strain

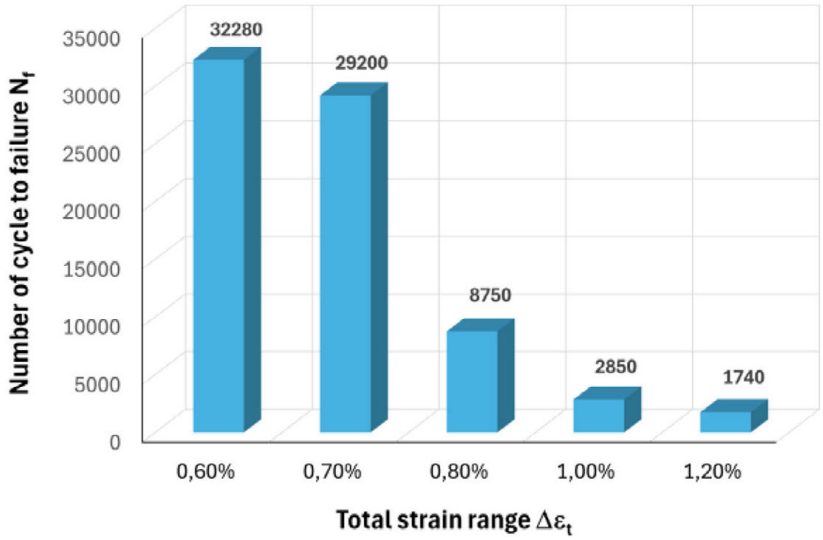

Figure 19. Fatigue life graph as a number of cycles to failure – negative values of total strain

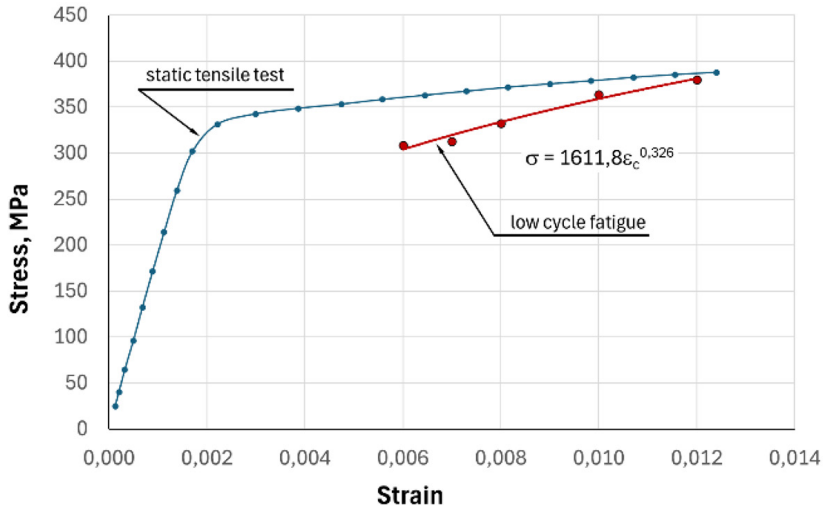

Figure 20. Cyclical strengthening chart – negative values of total strain

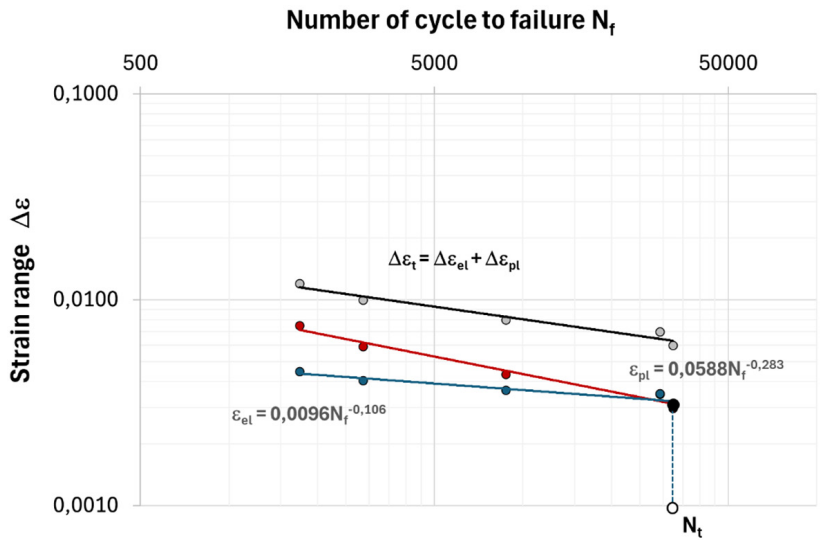

Figure 21. Manson-Coffin fatigue life diagram – negative values of total strain

The tested hogh manganese steel exhibited a prolonged stabilization period throughout all stages of testing (at strain ranges $\Delta\varepsilon_t$=0.6÷0.8%,). This was evident during both classical pendulum cycles and tests performed for positive and negative total strain ranges. This conclusion can be drawn from the σ=f(N) graphs. An example of the tests carried out in stage I is shown in Fig.23. The steel behaved similarly for the other stages of testing**.** Fatigue failure occurred in the last few tens of cycles. Analyzing the diagrams of cyclic strengthening (Figure 10, Figure 15, and Figure 20), different behavior was found depending on the realized stage of testing. Specimens subjected to LCF fatigue for oscilating cycles show cyclic weakening for small strain levels ($\Delta\varepsilon_t$=0.6÷0.8%) in the case of total strain of 1.0% and 1.2%, the steel showed cyclic strengthening. In the case of tests carried out for STAGE II (positive total strain level), the steel showed cyclic weakening, which for total strain ranges of 0.6÷0.8% was at about 50MPa. Only for the 1.2% strain range was there cyclic strengthening of about 20MPa from baseline. With regard to such studies, it can be pointed out that for austenitic but corrosion-resistant 316L steel as described in the paper [25] showed, for example, that the cyclic stress response of 316L stainless steel exhibits cyclic hardening, saturation and cyclic softening, and that the fatigue life of is negatively correlated with the strain amplitude.

For tests carried out at negative values of total strain (STAGE III), the material showed cyclic weakening. This was true for all realized strain levels. Based on the fatigue life diagrams in the Manson-Coffin system, we found that the position of the Nt point (the intersection of the plastic and elastic characteristics) significantly influences all fatigue test stages. For tests conducted in Stage I, we observed a greater influence of strength properties on low-cycle fatigue life. For tests conducted in stages II and III, plastic properties have a greater influence on low-cycle fatigue life. This is particularly evident in tests conducted at negative total strain, where the intersection of plastic and elastic fatigue characteristics occurred at the lowest total strain level achieved. Nevertheless, plastic properties were dominant in the failure process at each stage of testing. The analysis of the hysteresis loops for nearly all stages of testing reveals that X60MnAl20-3 steel exhibits a high degree of plasticity, as evidenced by the broad hysteresis loops and significant plastic deformation. This property is crucial for the application of this steel in elements within controlled crumple zones of car bodies, particularly during deformations with negative values.

Results of microstructure and fractographic analysis

In addition to the mechanical tests, fractographic studies of the fracture surface were conducted first (Figure 24–29). It can be concluded that, after static tensile testing, the steel exhibits the classic resolution fracture characteristic of ductile fracture. The fracture surface is homogeneous and contains visible craters and pits, as

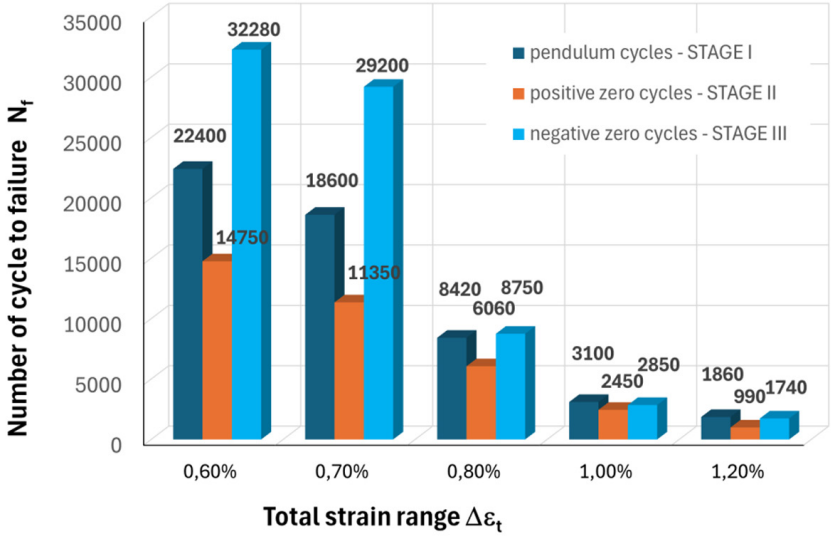

Figure 22. Comparison of fatigue life of X60MnAl20-3 steel for three stages of testing

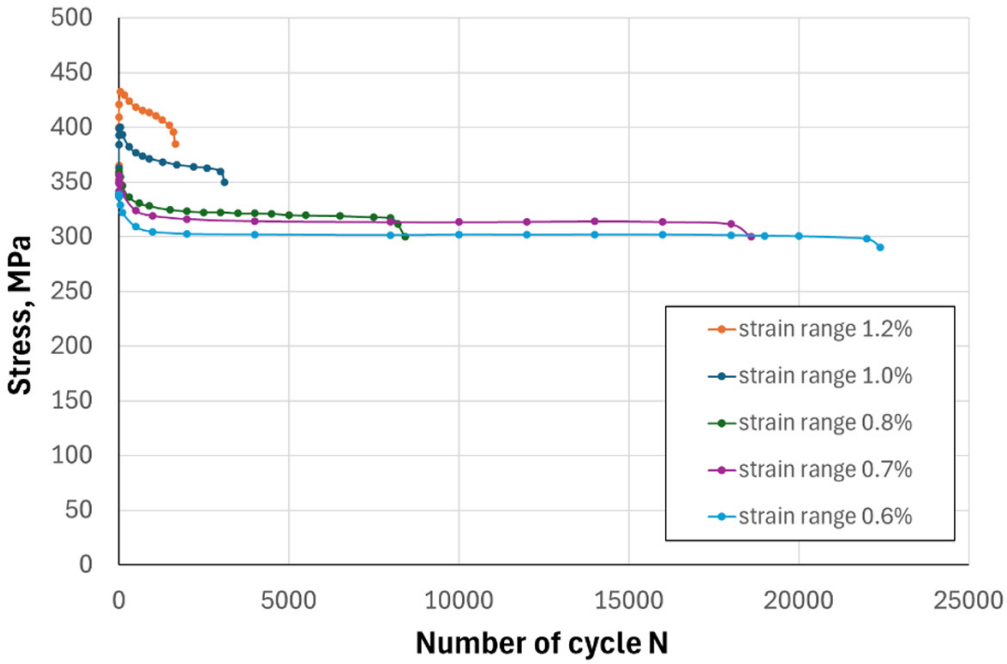

Figure 23. Cyclic strain graph – oscilating cycles, Stage I

well as the spiderweb pattern characteristic of ductile fractures. In fatigue tests performed at all stages (oscilating cycles, positive strain cycles, and negative strain cycles), the breakthroughs exhibit a uniform, pronounced ductile character. The ductile character of the breakthrough, evidenced by the presence of a spider web, numerous dimples, craters, and plastic striations, demonstrates the high ductility of the steel under fatigue loading conditions. It should be noted that, for all test stages I, II, and III, the plastic striations are more regular at lower total strain values (0.6%) and become less regular at higher strain values (1.2%).

After fatigue testing, the microstructure and the hardness of the tested steel was analyzed (Figure 30). It was observed that the microstructure is similar for test stages I, II, and III at lower total strain values of 0.6%. Numerous mechanical twins (MT) were observed in the austenite grains, which formed as a result of deformation. Their homogeneous distribution may reflect the similar strain distribution in the fracture area and the area away from the fracture point for strain ranges of 0.6% in Stages I, II, and III. The hardness tests analysis showed similar hardness value of tested steel for 0.6%, +0.6%, and -0.6% respectively 260HV1, 252HV1 and 246HV1. However, the situation is different for higher total strains of 1.2% in stages I, II, and III. The microstructure divides into two zones: an area of intense plastic deformation (area IPD), where twinning occurs more intensely, and an area of medium plastic deformation (area MPD), located about 0.5 mm from the fracture point, where twinning occurs less intensely. Upon analyzing the averaged hardness measurement

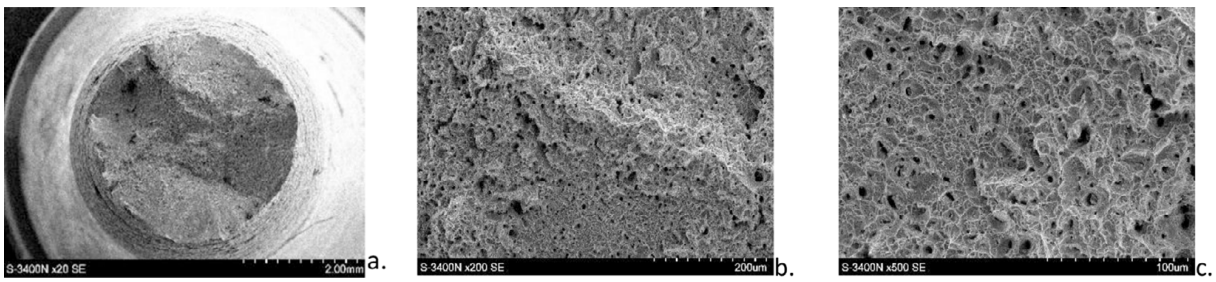

Figure 24. Microstructure of steel fracture after static tensile test, (a) general view, resolution fracture, (b, c) detailed view, plastic fracture, visible craters and pits, spider web characteristic of ductile fracture

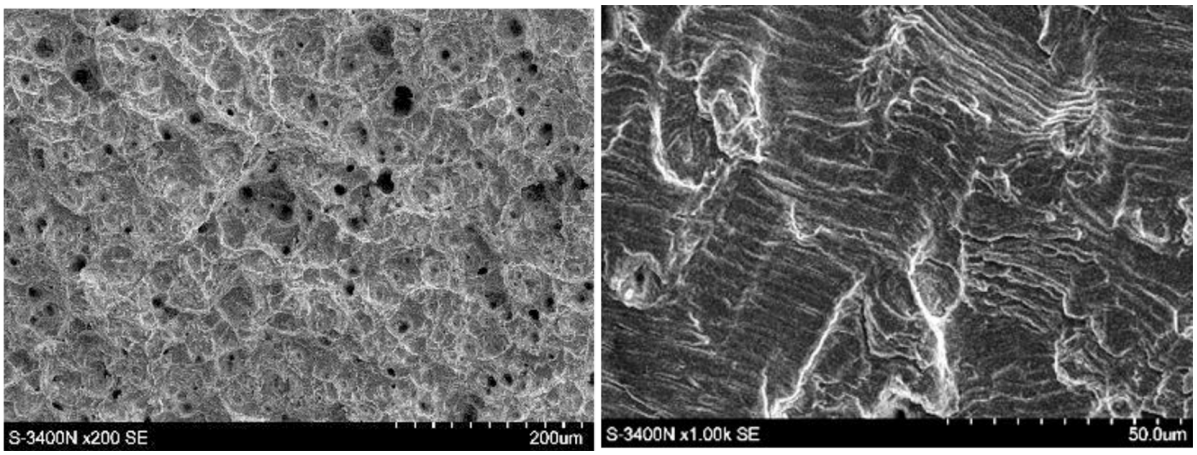

Figure 25. Steel fracture after STAGE I testing - total strain $\Delta\varepsilon_{\tau}$=0.6%

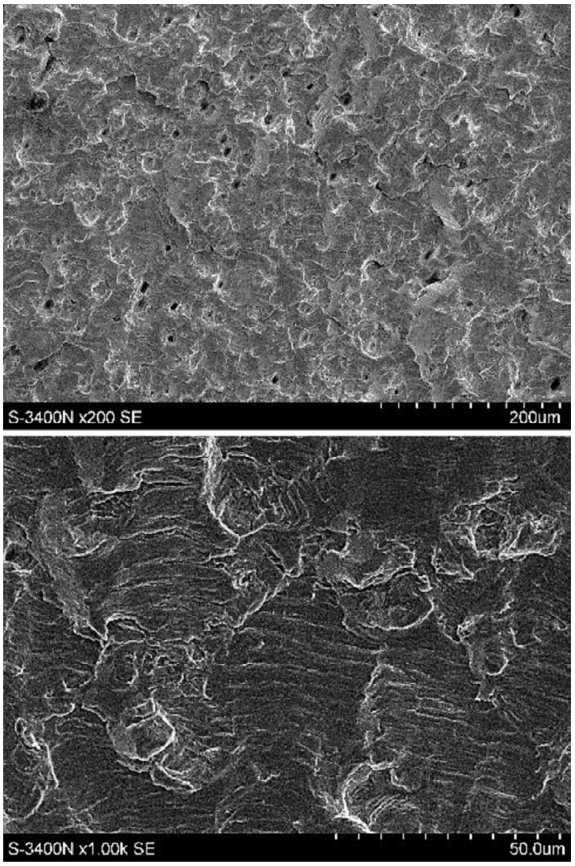

Figure 26. Steel fracture after STAGE II testing – total strain $\Delta\varepsilon_{t}$=+0.6%

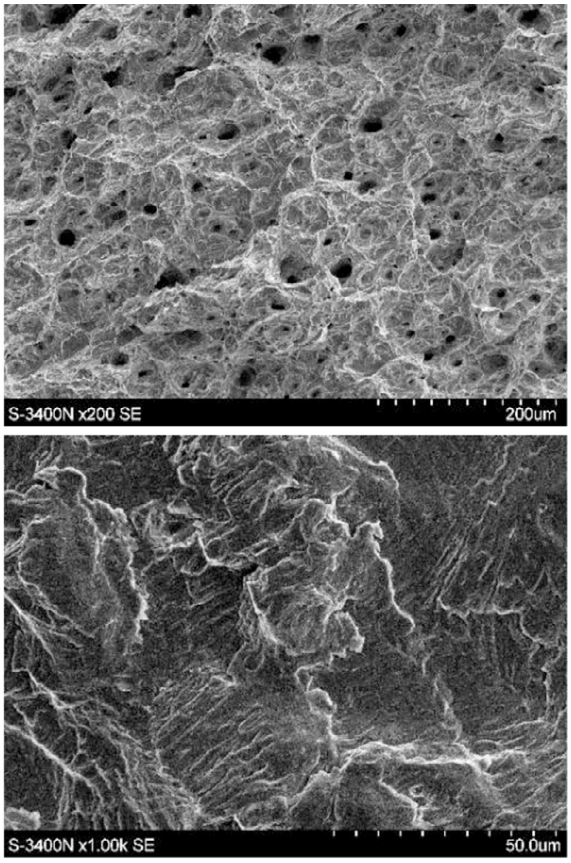

Figure 27. Steel fracture after STAGE III testing – total strain $\Delta\varepsilon_{t}$=-0.6%

results of the tested X60MnAl20-3 steel subjected to LCF within the high total strain range (1.2%), it can be concluded that the hardness is higher in the IPD zones than in the MDP zone. The hardness increases by 35 HV1 for total strain of +1.2% and by 24 HV1 for total strain of -1.2% in the areas closest to the fracture, where intense twinning is visible. According to the authors [12], the increase in hardness of TWIP steels, and thus their strengthening and increased fatigue resistance when subjected to cyclic fatigue, was noticeable and pronounced. This was particularly evident in coarse-grained steel due to repeated plastic deformation. As the authors mentioned in Steel X70MnAl17-2, twins are clearly visible as thin, reoriented lamellae. This

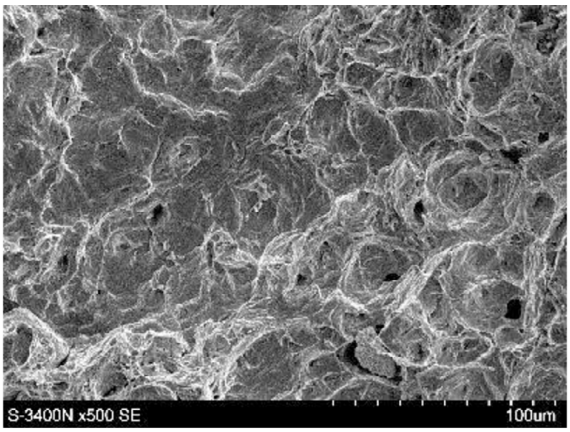

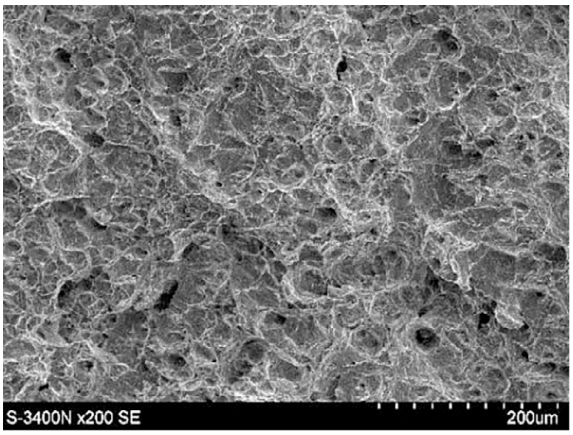

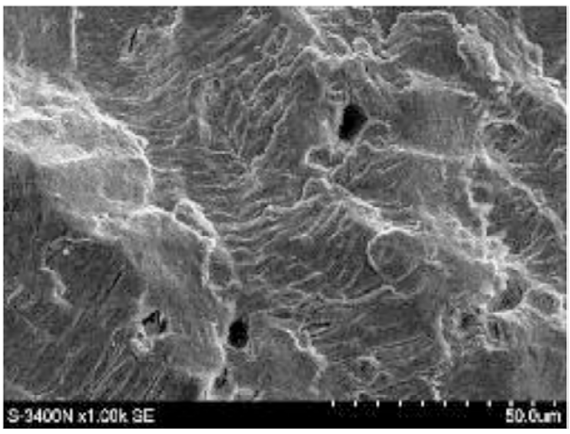

Figure 28. Steel fracture after STAGE II testing – total strain $\Delta\varepsilon_t$=+1.2%

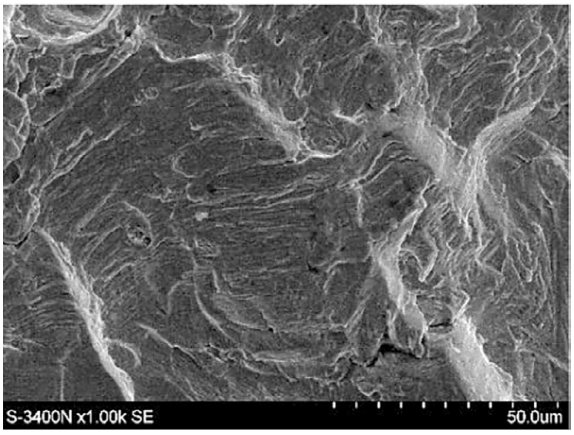

Figure 29. Steel fracture after STAGE III testing – total strain $\Delta\varepsilon_t$=-1.2%

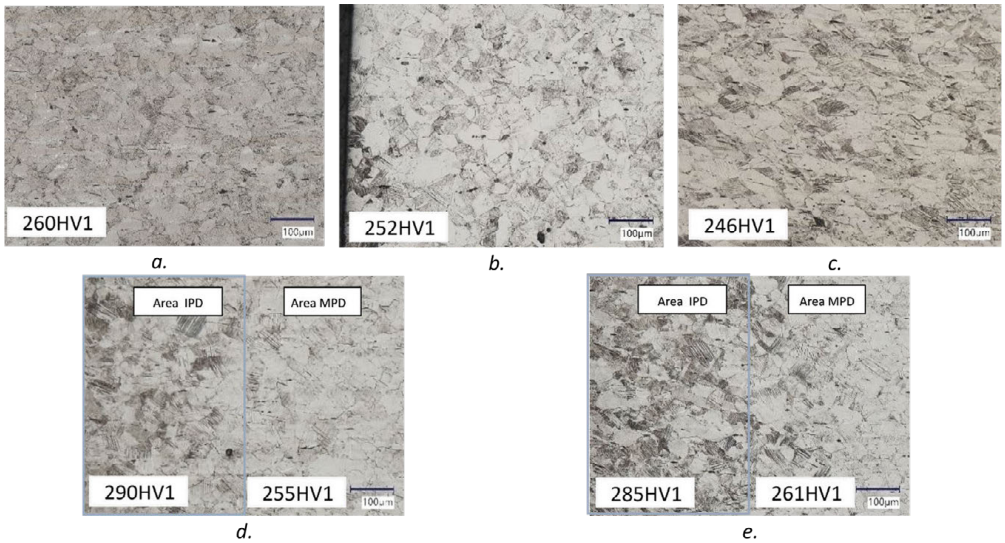

Figure 30. Microstructures and hardness results of the tested steel after fatigue tests, a. 0.6%, b. +0.6%, c. -0.6%, d. +1.2%, e. -1.2%

shows the massive deformation of the twins during the fatigue tests. This phenomenon indicates that the strain hardening and the superior ductility of TWIP steels due to the interaction of twins and dislocations. These phenomena are confirmed by the authors [26] in dynamic deformation tests, by the authors [27] in impact tests, and by the authors [13, 14] in fatigue tests.

CONCLUSIONS

1. The fatigue life of the tested X60MnAl20-3 TWIP steel strongly depends on the strain direction. The TWIP steel exhibited the longest fatigue life under negative total strain (STAGE III) and the lowest life under positive total strain (STAGE II). This indicates asymmetry in cyclic response, with the material being more sensitive to tensile deformation than compressive during LCF.
2. For lower total strain amplitudes (0.6-0.8%), the steel showed a deficiency during periods of fatigue cycles, especially in reversed and negative strain conditions. At higher strains (1.0–1.2%), cyclic hardening was observed, particularly evident in the reversed mode and at the highest positive strain level.
3. From the Manson-Coffin diagrams, it was found that in positive and negative strain cases (Stages II & III), plastic strain had a dominant influence on fatigue life, while for oscillating cycles (Stage I), strength properties played a more significant role in fatigue performance.
4. Fracture surfaces indicate high ductility. Fractographic analysis revealed that all fatigue failures were ductile, characterized by dimples, craters, and striations. This confirms that TWIP steel retains its excellent ductility even under cyclic loading, across all tested conditions.
5. Mechanical twinning is Active and localized. At low strains (0.6%), twinning was observed uniformly across the microstructure. At higher strains (1.2%), twinning was more intense near the fracture zone, confirming that twinning remains an active deformation mechanism in TWIP steel under LCF, especially in the intensely plastically deformed zones, contributing to cyclic strength and hardness increase.

Acknowledgements

The work was carried out under the IDUB-funded breakthrough research grant with the number 11/030/SDU/10-21-02.

REFERENCES

1. Chen S., Rana R., Haldar A., Ray R.K., Current state of Fe-Mn-Al-C low density steels, Prog. Mater. Sci. 89 (2017) 345e391. https://doi.org/10.1016/, j.pmatsci.2017.05.002.
2. De Cooman B.C., Estrin Y., Kim S.K. Twinning-induced plasticity (TWIP) steels. Acta Mater 2018; 142: 283–362. https://doi.org/10.1016/j.actamat.2017.06.046.
3. Chung K., Ahn K., Yoo D.-H., Chung K.-H., Seo M.-H., Park S.-H. Formability of TWIP (twinning induced plasticity) automotive sheets. Int J Plast 2011; 27(1): 52–81. https://doi.org/10.1016/j.ijplas.2010.03.006.
4. Grassel O., Krüger L., Frommeyer G., Meyer L.W. High strength Fe-Mn-(Al, Si) TRIP/ TWIP steels development - properties - application. Int J Plast 2000; 16(10–11): 1391–409. https://doi.org/10.1016/S0749-6419(00)00015-2.
5. Jabłońska, M.B., Effect of the conversion of the plastic deformation work to heat on the behaviour of TWIP steels: a review. Archiv.Civ.Mech. Eng; 2023; 23: 135. https://doi.org/10.1007/s43452-023-00656-0
6. Hwang S.W., Ji J.H., Park K.T., Effects of Al addition on high strain rate deformation of fully austenitic high Mn steels, Mater. Sci. Eng., 2011; *A*(528): 7267–7275, https://doi.org/10.1016/j.msea.2011.06.020.
7. Roa J.J., Fargas G., Calvo J., Jimenez-Pique E., Mateo A., Plastic deformation and damage induced by fatigue in TWIP steels, Mater. Sci. Eng. A. Struct. Mater. Prop. Microstruct. Process. 2015; 628: 410e418, https://doi.org/10.1016/ j.msea.2015.01.043.
8. Feng D., Li, Y., Song S., Liu Q., Bai Q., Ren F., Shangguan F., Influences of silicon on the work hardening behavior and hot deformation behavior of Fee25 wt% Mne(Si, Al) TWIP steel, J. Alloys Compd. 2015; 618: 768e775. https://doi.org/10.1016/j.jallcom.2014.08.239.
9. Jung I.C., Cho L., De Cooman B.C., In situ observation of the influence of Al on deformation-induced twinning in TWIP steel, ISIJ Int. 2015; 55: 870e876, https://doi.org/10.2355/isijinternational.55.870.
10. Park K.T., Jin K.G., Han S.H., Hwang S.W., Choi K., Lee C.S., Stacking fault energy and plastic deformation of fully austenitic high manganese steels: effect of Al addition, Mater. Sci. Eng. 2010; 527: 3651e3661. https://doi.org/10.1016/j.msea.2010.02.058.
11. Luo Z.C., Liu R.D., Wang X., Huang M.X. The effect of deformation twins on the quasicleavage crack propagation in twinning-induced plasticity steels. Acta Mater. 2018; 150: 59–68. https://doi.org/10.1016/j.actamat.2018.03.004.
12. Hamada A.S., Karjalainen L.P., Puustinen J., Fatigue behavior of high-Mn TWIP steels, Mater. Sci. Eng. 2009; 517: 68e77, https://doi.org/10.1016/j.msea.2009.03.039.
13. Hamada A.S., Karjalainen L.P., Ferraiuolo A., Gil

Sevillano J., De Las Cuevas F., Pratolongo G., Reis M., Fatigue behavior of four high-Mn twinning induced plasticity effect steels, Metall. Mater. Trans. A Phys. Metall. Mater. Sci. 2010; 41: 1102e1108. https://doi.org/10.1007/s11661-010-0193-7.

14. Niendorf T., Lotze C., Canadinc D., Frehn A., Maier H.J., The role of monotonic pre-deformation on the fatigue performance of a high-manganese austenitic TWIP steel, Mater. Sci. Eng. 2009; 499: 518e524, https://doi.org/10.1016/j.msea.2008.09.033.
15. Seo W., Jeong D., Sung H., Kim S., Tensile and high cycle fatigue behaviors of high-Mn steels at 298 and 110 K, Mater, Character. 2017; 124: 65e72, https://doi.org/10.1016/j.matchar.2016.12.001.
16. Cornette D., Cugy P., Hildenbrand A., Bouzekri M., Lovato G. Aciers` a tr`es haute r´esistance FeMn TWIP pour pi`eces de s´ecurit´e dans la construction automobile. Rev Metall Cah D'Informations Tech. 2005; 102: 905–18. https://doi.org/10.1051/metal:2005151.
17. Fleck N.A., Kang K.J., Ashby M.F. Overview no. 112. The cyclic properties of engineering materials. Acta Metall Mater. 1994; 42: 365–81. https://doi.org/10.1016/0956-7151(94)90493-6.
18. Karjalainen L.P., Hamada A., Misra R.D.K., Porter D.A. Some aspects of the cyclic behavior of twinning-induced plasticity steels. Scr Mater 2012; 66(12): 1034–9. https://doi.org/10.1016/j.scriptamat.2011.12.008
19. Gui L.M., Jin X.C., Li H.T., Zhang M. High cycle fatigue performances of advanced high strength steel CP800. Adv Mater Res, Trans Tech Publications Ltd. 2014; 238–41. https://doi.org/10.4028/www.scientific.net/AMR.989-994.238.
20. Lara A., Picas I., Casellas D. Effect of the cutting process on the fatigue behaviour of press hardened and high strength dual phase steels. J Mater Process Technol 2013; 213(11): 1908–19. https://doi.org/10.1016/j.jmatprotec.2013.05.003.
21. Parareda S., Casellas D., Frometa ´ D., Martínez M., Lara A., Barrero A., et al. Fatigue resistance of press hardened 22MnB5 steels. Int J Fatigue 2020; 130: 105262. https://doi.org/10.1016/j.ijfatigue.2019.105262.
22. Junak G., Marek A., Paduchowicz M., Impact of temperature on low-cycle fatigue characteristics of the HR6W alloy. Materials, ISSN 1996-1944. DOI:10.3390/ma14226741. 2021.
23. Okrajni J., Wacławiak K., Junak G., Twardawa M., Stress–strain behavior and fatigue of high-temperature component made of P92 steel in a coal-fired power boiler. Energies, 1996–1073. https://doi.org/10.3390/en17122870.2024.
24. Yin T.W., Shen Y.F., Xue W.Y., Jia N., Zuo L., Ce addition enabling superior strength and ductility combination of a low-carbon low-manganese transformation-induced plasticity steel, Mater. Sci. Eng. 2022; A 849. https://doi. org/10.1016/j.msea.2022.143474.
25. Lesiuk G., Rozumek D., Fracture Mechanics and Fatigue Damage of Materials and Structures, Materials. 2023; 16: 4171, https://doi.org/10.3390/ma16114171.
26. Jabłońska M., Śmiglewicz A. Analysis of substructure of high-Mn steels in the context of dominant stress mechanism, 8th International Conference on Diffusion in Solids Liquids, Defect and Diffusion Forum, 2013, Stafa, Trans Tech Publications. 2013; 334–335: 177–181. https://doi.org/10.4028/www.scientific.net/DDF.334-335.177.
27. Śmiglewicz A., Jabłońska M., The effect of strain rate on the impact strength of the high-Mn steel, Metalurgija, 2015; 54(4): 631–634.